Representing molecular ground and excited vibrational eigenstates with nuclear densities obtained from semiclassical initial value representation molecular dynamics

The Journal of Chemical Physics

Representing molecular ground and excited vibrational eigenstates with nuclear densities obtained from semiclassical initial value representation molecular dynamics

Cite as: J. Chem. Phys. **153**, 214117 (2020); https://doi.org/10.1063/5.0031391
Submitted: 30 September 2020 . Accepted: 11 November 2020 . Published Online: 07 December 2020

Chiara Aieta, Gianluca Bertaina, Marco Micciarelli, and Michele Ceotto

The Journal of Chemical Physics ARTICLE scitation.org/journal/jcp

Representing molecular ground and excited vibrational eigenstates with nuclear densities obtained from semiclassical initial value representation molecular dynamics

Cite as: J. Chem. Phys. 153, 214117 (2020); doi: 10.1063/5.0031391
Submitted: 30 September 2020 • Accepted: 11 November 2020 •
Published Online: 7 December 2020

Chiara Aieta,[1] Gianluca Bertaina,[1,2] Marco Micciarelli,[1,a)] and Michele Ceotto[1,b)]

AFFILIATIONS

[1] Dipartimento di Chimica, Università degli Studi di Milano, Via C. Golgi 19, 20133 Milano, Italy
[2] Istituto Nazionale di Ricerca Metrologica, Strada delle Cacce 91, 10135 Torino, Italy

Note: This paper is part of the JCP Special Topic on Quantum Dynamics with *Ab Initio* Potentials.
[a)] marco.miccia@gmail.com
[b)] **Author to whom correspondence should be addressed:** michele.ceotto@unimi.it

ABSTRACT

We present in detail and validate an effective Monte Carlo approach for the calculation of the nuclear vibrational densities via integration of molecular eigenfunctions that we have preliminary employed to calculate the densities of the ground and the excited OH stretch vibrational states in the protonated glycine molecule [Aieta *et al.*, Nat Commun **11**, 4348 (2020)]. Here, we first validate and discuss in detail the features of the method on a benchmark water molecule. Then, we apply it to calculate on-the-fly the *ab initio* anharmonic nuclear densities in the correspondence of the fundamental transitions of NH and CH stretches in protonated glycine. We show how we can gain both qualitative and quantitative physical insight by inspection of different one-nucleus densities and assign a character to spectroscopic absorption peaks using the expansion of vibrational states in terms of harmonic basis functions. The visualization of the nuclear vibrations in a purely quantum picture allows us to observe and quantify the effects of anharmonicity on the molecular structure, also to exploit the effect of IR excitations on specific bonds or functional groups, beyond the harmonic approximation. We also calculate the quantum probability distribution of bond lengths, angles, and dihedrals of the molecule. Notably, we observe how in the case of one type of fundamental NH stretching, the typical harmonic nodal pattern is absent in the anharmonic distribution.

I. INTRODUCTION

Visualizing molecular vibrations in real time and at the atomistic length scale would be of great importance to understand chemical phenomena. Experiments can usually access molecular motions only in an indirect way. Even if modern vibrational spectroscopies are so sophisticated as to probe isolated molecules,[1–7] only vibrational frequencies are routinely measured. Information about vibrational motion is extracted from the spectra via the assignment of the peaks. In this way, for instance, it has been possible to elucidate the structure of biomolecule conformers,[8] characterize the intermediates in chemical reactions,[9,10] help the rationalization of weak interactions such as H-bonds,[11] and support the understanding of solvation.[12–14] However, this spectroscopic procedure sometimes does not bring to undisputed interpretations.[15,16] To directly observe molecular vibrations, it would be necessary to push the limit of spatial and energy resolution of experimental spectroscopy. A technique that evolved in this direction is the Tip-Enhanced Raman Spectroscopy (TERS).[17–19] Recently, a TERS experiment has produced two-dimensional spatial images at Ångström-scale resolution, where the peaks correlate with the intensity and direction of vibrational normal-mode displacements.[20] Also, data from elastic scattering of x-ray generated with a Free-Electron Laser (XFEL) source can be opportunely treated to get diffraction

images of specific vibrational states of molecules in the gas phase.[21]

Alongside experimental techniques, a complementary way to get atomistic insight into molecular motions is provided by computer simulations. Theoretical chemistry methods usually simulate molecular vibrations under the Born–Oppenheimer (BO) approximation. The dynamics of a bound state on the BO Potential Energy Surface (PES) is usually treated in the small oscillation regime. This approach approximates the potential in the surroundings of a minimum as a quadratic function of the coordinates, and the normal-mode picture for vibrations is introduced. Several methodologies have been developed to project normal-mode motions onto chemically meaningful internal coordinates, such as bond lengths, angles, and dihedrals, in the most unambiguous way possible.[22] However, these methods for the visualization of nuclear motion completely overlook the effects derived from the quantum nature of the nuclei.

Solving the nuclear time-independent Schrödinger equation from direct diagonalization of the exact molecular Hamiltonian to get the vibrational eigenfunction can be achieved only for low-dimensional systems. For larger systems, it is necessary to develop specific methodologies to account for anharmonicity and coupling between modes in the ground and excited vibrational states.[23–33] Then, even if one is able to get the eigenfunctions, a further issue is how to better visualize them and get physical information. For N-atom molecules, the vibrational eigenfunctions have a $3N - 6$ dimensionality or $3N - 5$ if the molecule has a linear shape. As a consequence, such wavefunctions are usually analyzed by plotting bidimensional cuts along some selected pairs of normal modes bringing some information.[34] For example, the presence of nodal planes in these contour plots and their tilted shape reveal the resonance and anharmonic couplings between normal modes.[35] Visualizing directly the vibrational behavior of molecules in three-dimensional space in the quantum picture would boost our physical insight.

Very recently, the analysis of quantum one-nucleus densities, i.e., the probability of finding each nucleus in a molecule at a given position in space independent of the location of the others, has been proposed as a tool to get information about molecular normal modes from the wavefunction.[36] In that work, harmonic one-nucleus densities were computed by analytic integration of the harmonic eigenfunctions. The focus was on how the wavefunction nodal structure of the vibrationally excited states is reflected in the one-nucleus density. It was found that only certain vibrational excitations change the one-nucleus density qualitatively as compared to the ground state. Alternatively, one can partially represent the density by including the lighter nuclei in the electronic structure calculation.[37]

In our previous work,[38] we further advanced the investigation of one-nucleus densities. More specifically, we introduced a well-controlled Monte Carlo integration to compute expectation values of the nuclear density operators from anharmonic vibrational molecular eigenstates written on a basis of harmonic states. As a first application, we estimated the expansion coefficients for the ground and excited OH stretch eigenfunctions of protonated glycine beyond the harmonic approximation with a semiclassical technique recently developed in our group.[39] We represented one-nucleus densities with the cube file format, which can be visualized with 3D graphics programs,[40] as it is customarily done for electron density and orbitals. Comparison between the isosurface plots of harmonic and anharmonic vibrational densities permits us to visualize molecular geometries and vibrations from a quantum mechanical point of view.

In this work, we include anharmonicity effects through the Multiple Coherent states Time Averaged Semiclassical Initial Value Representation (MC SCIVR)[41–48] in which a semiclassical propagator is obtained by stationary phase approximation of the exact Feynman's path integral formulation.[49] Recently, semiclassical initial value representation techniques have advanced the field of spectroscopy simulations,[50–52] including temperature-dependent spectra.[39,53,54] The MC SCIVR employs information obtained by processing few classical trajectories either on the adiabatic electronic PES or on-the-fly. Moreover, with this technique, the anharmonic excited states are obtained at the same cost of the ground-state wavefunction. MC SCIVR had been successfully applied for power spectra calculations, i.e., eigenvalue calculations, to a number of medium- and large-size molecular systems such as fullerene,[55] glycine,[56] benzene,[57] water clusters,[58] pre-reactive complexes,[59] system–bath models,[60–62] the protonated glycine dimer and H_2-tagged protonated glycine,[16] nucleobases and nucleosides,[63,64] and the Zundel cation[65] and more recently to surface adsorbed molecules.[66]

In this paper, we calculate the one-nucleus densities and density differences and discuss the shape and the nodal structure of the corresponding excited states with an extensive application on the water molecule as a benchmark and protonated glycine to complement the already investigated excited OH stretch nuclear density.[38] Specifically, the differences between anharmonic and harmonic wavefunctions with the same degree of excitation highlight the effect of anharmonicity and the relevant consequences on the molecular structure (probability distributions of bond lengths, angles, and dihedrals). In addition, we investigate the character of vibrational excitations by considering differences between the excited and the ground-state densities. In the harmonic picture, we propose this as an alternative way to intuitively visualize normal-mode displacements without resorting to a classical interpretation based on classical trajectories visualization. In the anharmonic framework, these differences reveal the non-local nature of vibrational excitations, which are directly associated with the peaks observed in vibrational spectroscopy, going beyond the simplified harmonic normal-mode picture.

This paper starts with the definition of the density distributions and the description of the numerical approach we use to calculate them. In Sec. II, we recall the semiclassical technique based on MC SCIVR, which allows the calculation of the ground and excited state semiclassical vibrational eigenfunctions. Next, we move on to the presentation of the results for two representative cases (Sec. III). We compute densities for the water molecule, for which we calculate the exact values on the same fitted PES. We use this system to validate our approach. In Sec. III B, we move to the protonated glycine ($GlyH^+$), a moderate dimensionality molecule containing 11 atoms for which a fitted PES is not available. This molecule is interesting for future study of molecular solvation, as suggested by IR spectroscopy results.[12,67] Finally, in Sec. IV, we provide the conclusions and future development outlook.

II. THEORY

A. Molecular nuclear densities

Under the BO approximation, an N-atom molecule can be described by considering the spectral decomposition of the nuclear Hamiltonian operator $\hat{H}|e_n\rangle = E_n|e_n\rangle$, where the nuclear eigenfunctions are denoted by $|e_n\rangle$ and E_n is the corresponding eigenvalue.

By diagonalizing the mass-scaled potential Hessian matrix at equilibrium, the diagonal matrix $\mathbf{\Gamma}$ of the eigenvalues ω_α ($\alpha = 1, \ldots, 3N$) is obtained, as well as the conversion matrix between the Cartesian and the normal-mode coordinates $\mathbf{Q}$. In this work, we analytically determine the roto-translational modes $\boldsymbol{Q}^{RT}$, which we keep fixed at their null equilibrium position, and perform a Gram–Schmidt orthogonalization of the remaining N_v vibrational modes.[65,68] This small-displacement approximation is commonly used and corresponds to separating vibrations and rotations, specifically to neglect their coupling. When the system lies in the n-th eigenstate $|e_n\rangle$, the quantum probability density distribution of a generic physical quantity $\boldsymbol{\theta}(\boldsymbol{Q})$ is then computed as

$$\rho_{n,\boldsymbol{\theta}}(\boldsymbol{x}) = \int d^{3N}\boldsymbol{Q}|\langle \boldsymbol{Q}|e_n\rangle|^2 \delta(\boldsymbol{Q}^{RT})\delta(\boldsymbol{\theta}(\boldsymbol{Q}) - \boldsymbol{x}), \tag{1}$$

where $\boldsymbol{x}$ is a vector variable of the same dimensionality as $\boldsymbol{\theta}$.

Numerically, we represent the $\rho_{n,\boldsymbol{\theta}}(\boldsymbol{x})$ density as a histogram divided into B bins of volume Ω and centered around the $\mathbf{x}^j$ ($j = 1, \ldots, B$) positions. Therefore, the average value of $\rho_{n,\boldsymbol{\theta}}(\boldsymbol{x})$ in the j-th bin is

$$\bar{\rho}^{\,j}_{n,\boldsymbol{\theta}} = \frac{1}{\Omega}\int d^{3N}\boldsymbol{Q}|\langle \boldsymbol{Q}|e_n\rangle|^2 \delta(\boldsymbol{Q}^{RT}) I^j_{\boldsymbol{\theta}}(\boldsymbol{Q}), \tag{2}$$

where, for a given coordinate $\boldsymbol{Q}$, the index function $I^j_{\boldsymbol{\theta}}(\boldsymbol{Q})$ is equal to 1 if $\boldsymbol{\theta}(\boldsymbol{Q})$ belongs to the bin centered around $\mathbf{x}^j$, while it is null otherwise. The density normalization condition imposes the following normalization over its histogram representation: $\Omega\sum_j \bar{\rho}^{\,j}_{n,\boldsymbol{\theta}} = 1$. The calculation of the integral in Eq. (2) is particularly suited for its evaluation via simple Gaussian Monte Carlo sampling. Thanks to the separation of vibrations from rotations and translations, the eigenfunctions are expanded in the basis of the harmonic vibrational states $|\phi_{\boldsymbol{K}}\rangle$ as

$$|e_n\rangle = \sum_{\boldsymbol{K}} C_{n,\boldsymbol{K}}|\phi_{\boldsymbol{K}}\rangle. \tag{3}$$

Here, $\boldsymbol{K} = (K_1, \ldots, K_{N_v})$ are positive integer vectors, indicating the excitation degree of each harmonic vibrational mode. The harmonic case is simply retrieved by considering $C_{n,\boldsymbol{K}} = \delta_{\bar{\boldsymbol{K}},\boldsymbol{K}}$. In coordinate representation, one can factor out the Gaussian terms as $\langle \boldsymbol{Q}|e_n\rangle = G(\mathbf{Q},\mathbf{\Gamma})\sum_{\mathbf{K}} C_{n,\mathbf{K}}\,\tilde{\phi}_{\mathbf{K}}(\mathbf{Q})$, where $G(\mathbf{Q},\mathbf{\Gamma}) = |\mathbf{\Gamma}/(\pi\hbar)|^{1/4}\exp\left(-\mathbf{Q}^T\mathbf{\Gamma}\mathbf{Q}/(2\hbar)\right)$ and $\tilde{\phi}_{\mathbf{K}}(\mathbf{Q}) = \prod_{\alpha=1}^{N_v}\left(2^{K_\alpha}K_\alpha!\right)^{-1/2} \times h_{K_\alpha}\left(\sqrt{\omega_\alpha/\hbar}\,Q_\alpha\right)$, with the $K^{th}{}_\alpha$-order Hermite polynomial denoted as h_{K_α}. Thanks to this factorization, Eq. (2) can be conveniently recast as

$$\bar{\rho}^{\,j}_{n,\boldsymbol{\theta}} = \frac{1}{\Omega}\int \left[d^{3N}\mathbf{Q}\,|G(\mathbf{Q},\mathbf{\Gamma})|^2\right] \times \left|\sum_{\mathbf{K}} C_{n,\mathbf{K}}\tilde{\phi}_{\mathbf{K}}(\mathbf{Q})\right|^2 \delta(\mathbf{Q}^{RT}) I^j_{\boldsymbol{\theta}}(\boldsymbol{Q}). \tag{4}$$

Eventually, we generate a set of independent L molecular configurations along a multivariate Gaussian distribution with the null mean and variance equal to $(2\mathbf{\Gamma}/\hbar)^{-1}$ for the vibrational modes only by means of the Box–Muller algorithm,[69] and we evaluate the integral in Eq. (4) as

$$\bar{\rho}^{\,j}_{n,\boldsymbol{\theta}} = \lim_{L\to\infty}\frac{1}{\Omega L}\sum_{l=1}^{L}\left|\sum_{\mathbf{K}} C_{n,\mathbf{K}}\tilde{\phi}_{\mathbf{K}}(\mathbf{Q}_l)\right|^2 I^j_{\boldsymbol{\theta}}(\mathbf{Q}_l). \tag{5}$$

Since the function $\boldsymbol{\theta}(\boldsymbol{Q})$ is always an analytical expression of the nuclear coordinates, the computation of Eq. (4) is computationally cheap, once the anharmonic expansion coefficients $C_{n,\mathbf{K}}$ are known for a given vibrational state n. Also, the values of $\tilde{\phi}_{\mathbf{K}}(\mathbf{Q}_l)$ are analytical and can be easily evaluated over a large number of configurations (usually in the order of $L = 10^8$) with limited computational overhead. By only sampling the common Gaussian term, all samples are uncorrelated, and physical quantities relative to multiple excited states can be sampled at once, unlike the diffusion Monte Carlo algorithm that can measure quantities only in the ground state or in states with a predetermined nodal surface.[28,29] All calculations in this work are converged in order to have statistical error bars that are not visible in the plots. The error bar of the quantities is estimated in the standard way as the square root of the variance divided by L.

When $\boldsymbol{\theta} = \boldsymbol{R}_i$, where $\boldsymbol{R}_i$ is the Cartesian position of the i-th nucleus, the probability density of Eq. (1) assumes the form

$$\rho_{n,\boldsymbol{R}_i}(\boldsymbol{R}) = \int d^{3N}\boldsymbol{Q}|\langle \boldsymbol{Q}|e_n\rangle|^2 \delta(\boldsymbol{Q}^{RT})\delta(\boldsymbol{R}_i(\boldsymbol{Q}) - \boldsymbol{R}), \tag{6}$$

which corresponds to the marginal i-th one-nucleus density,[36] which is the nuclear analogue of electron density of density functional theory for electronic structure calculations.[70] Due to the larger mass of the nuclei as compared to electrons, the one-nucleus densities are sufficiently localized so that the overlap of densities of different nuclei in the molecule is negligible. Therefore, we can consider the one-nucleus density for a molecule,

$$\rho_n(\boldsymbol{R}) = \sum_{i=1}^{N}\rho_{n,\boldsymbol{R}_i}(\boldsymbol{R}), \tag{7}$$

which is defined in Cartesian coordinate space[36] and allows for the visualization of its 3D isosurfaces, as it is commonly done for electronic structure calculations.

In this work, we also evaluate bond-length quantum distributions by considering $\theta = |\boldsymbol{r}_{ij}|$, where $\boldsymbol{r}_{ij} \equiv \boldsymbol{R}_i - \boldsymbol{R}_j$ for all pairs of nuclei i and j, and angle quantum distributions by using $\theta = \arccos(\hat{\boldsymbol{r}}_{ik}\cdot\hat{\boldsymbol{r}}_{jk})$ for all triplets of nuclei i, j, and k forming an angle with vertex k, with $\hat{\boldsymbol{r}}_{ij} \equiv \boldsymbol{r}_{ij}/|\boldsymbol{r}_{ij}|$. Finally, we evaluate dihedral quantum distributions for quadruplets of atoms i, j, k, and l by considering $\theta = \arctan 2(s, c)$, with $s = [(\hat{\boldsymbol{r}}_{ji}\times\hat{\boldsymbol{r}}_{kj})\times(\hat{\boldsymbol{r}}_{kj}\times\hat{\boldsymbol{r}}_{lk})]\cdot\hat{\boldsymbol{r}}_{kj}$ and $c = (\hat{\boldsymbol{r}}_{ji}\times\hat{\boldsymbol{r}}_{kj})\cdot(\hat{\boldsymbol{r}}_{kj}\times\hat{\boldsymbol{r}}_{lk})$.[71]

B. MC-SCIVR anharmonic eigenfunctions

To calculate the coefficients $C_{n,\mathbf{K}}$ of Eq. (3), we employ our recently developed semiclassical method,[39,53] which is summarized in this section.

The eigenvectors of a generic Hamiltonian $\hat{H}$ are a complete basis set, and the spectroscopic weight of a given state $|\chi\rangle$ at the energy of each eigenvalue E_n, i.e., $|\langle\chi|e_n\rangle|^2$, can be obtained from the

following Fourier transform:

$$\begin{aligned}\tilde{I}_\chi(E) &= \frac{1}{\pi\hbar} Re \int_0^\tau dt \langle\chi|e^{-\frac{i}{\hbar}\hat{H}t}|\chi\rangle e^{\frac{i}{\hbar}Et} \\ &= \frac{1}{\pi\hbar} Re \int_0^\tau dt \sum_n \langle\chi|e_n\rangle e^{-\frac{i}{\hbar}E_n t}\langle e_n|\chi\rangle e^{\frac{i}{\hbar}Et} \\ &= \sum_n |\langle\chi|e_n\rangle|^2 \mathcal{D}(E-E_n;\Delta_\tau). \end{aligned} \tag{8}$$

In Eq. (8), the dynamical convolution function $\mathcal{D}$ is a nascent delta function, i.e., one of the functions belonging to the sequence of functions approaching, in the weak sense, the Dirac delta distribution, with peak centered on E_n with width Δ_τ approaching zero as the simulation time $\tau \to \infty$. We derive the Hamiltonian eigenvalues from the positions of the spectral peaks, while the squared projections $|\langle\chi|e_n\rangle|^2$ of the reference state onto the eigenvectors are determined from their peak intensities. Specifically, the harmonic weights of Eq. (3) can be written as $|C_{n,\mathbf{K}}|^2 \propto \tilde{I}_{\phi_\mathbf{K}}(E_n)$. As shown in detail in our previous work,[39] the signed $C_{n,\mathbf{K}}$ coefficients can be calculated from survival amplitudes using the following formula:

$$C_{n,\mathbf{K}} = \frac{\Delta\tilde{I}_{\phi_\mathbf{0},\phi_\mathbf{K}}(E_n)}{2\sqrt{\tilde{I}_{\phi_\mathbf{0}}(E_n)}}, \tag{9}$$

where $\phi_\mathbf{0}$ is the harmonic ground state, $\tilde{I}_{\phi_\mathbf{K}}(E_n)$ is the value at energy E_n of the power spectrum obtained with the harmonic state $|\phi_\mathbf{K}\rangle$, and

$$\Delta\tilde{I}_{\phi_{\mathbf{K}_1},\phi_{\mathbf{K}_2}}(E) \equiv \tilde{I}_{\phi_{\mathbf{K}_1}+\phi_{\mathbf{K}_2}}(E) - \tilde{I}_{\phi_{\mathbf{K}_1}}(E) - \tilde{I}_{\phi_{\mathbf{K}_2}}(E). \tag{10}$$

We obtain the quantum time evolution and the Fourier transform in Eq. (8) by using the MC-SCIVR approach, which relies on the evolution of just a handful of selected classical trajectories with initial conditions $\left(\mathbf{Q}_0^{(n)}, \mathbf{P}_0^{(n)}\right)$.[43–45,56] These are tailored to ideally correspond to the nth vibrational state via the Einstein–Brillouin–Keller (EBK) rules,

$$\oint_{H\left(\mathbf{Q}_0^{(n)},\mathbf{P}_0^{(n)}\right)=E_n} \boldsymbol{P}^{(n)} d\boldsymbol{Q}^{(n)} = \hbar\left(\zeta_n + \frac{\mu_n}{4}\right), \tag{11}$$

where ζ_n are positive integers and μ_n are Maslov indexes.[72] In the separable case, these rules provide a link between the n-th vibrational state and a N_v-dimensional vector of natural numbers $\boldsymbol{v}$ such that $\zeta_n = \sum_\alpha v_\alpha$, which is valid also beyond the harmonic approximation. In the MC-SCIVR approach, these classical trajectories are chosen with the total energy (also energy partition) corresponding to the harmonic oscillator spectral energies $E_v^{HO} = \sum_\alpha (1/2 + v_\alpha)\hbar\omega_\alpha$ and are generated by considering the initial conditions

$$\begin{aligned} Q_{0,\alpha}^{(n)} &= \sqrt{\frac{\hbar(2v_\alpha+1)}{\omega_\alpha}}\sin(\delta_\alpha), \\ P_{0,\alpha}^{(n)} &= \sqrt{(2v_\alpha+1)\hbar\omega_\alpha}\cos(\delta_\alpha), \end{aligned} \tag{12}$$

where the equilibrium position is located at the origin and the angles δ_α govern the partition of the starting energy of the α-th normal mode into potential and kinetic terms.

In this framework, the power spectrum of the survival amplitude of a generic state $|\chi\rangle$ is computed from the classical evolution of a single trajectory as[41,42]

$$\tilde{I}_{v,\chi}(E) \propto \frac{1}{\tau}\left|\int_0^\tau dt \langle\chi|\mathbf{Q}_t^{(n)},\mathbf{P}_t^{(n)}\rangle e^{i[S_t^{(n)}+\phi_t^{(n)}+Et]/\hbar}\right|^2. \tag{13}$$

When $|\chi\rangle = |\phi_K\rangle$, the factor $\langle\chi|\mathbf{Q}_t^{(n)},\mathbf{P}_t^{(n)}\rangle$ is analytical, and we get

$$|C_{n,\mathbf{K}}|^2 \propto \tilde{I}_{\phi_\mathbf{K}}(E_n) \simeq \tilde{I}_{v,\phi_\mathbf{K}}(E_n). \tag{14}$$

In Eq. (13), the coherent states $|\boldsymbol{Q},\boldsymbol{P}\rangle$ have the following normal-mode coordinate representation:[73–75]

$$\langle\boldsymbol{x}|\boldsymbol{Q},\boldsymbol{P}\rangle = \left|\frac{\boldsymbol{\Gamma}}{\pi\hbar}\right|^{\frac{1}{4}} e^{-\frac{1}{2\hbar}(\boldsymbol{x}-\mathbf{Q})^T\boldsymbol{\Gamma}(\boldsymbol{x}-\mathbf{Q})+\frac{i}{\hbar}\mathbf{P}(\boldsymbol{x}-\mathbf{Q})}, \tag{15}$$

where $S_t^{(n)}$ is the classical action of the trajectory at time t and $\phi_t^{(n)}$ is the phase of the Herman–Kluk prefactor $C_t^{(n)}$.[76–84] The latter accounts for quantum fluctuations and is defined as

$$C_t^{(n)} = \left|\frac{1}{2}\left(\boldsymbol{M}_{\boldsymbol{QQ}} + \boldsymbol{\Gamma}^{-1}\boldsymbol{M}_{\boldsymbol{PP}}\boldsymbol{\Gamma} - i\boldsymbol{M}_{\boldsymbol{QP}}\boldsymbol{\Gamma} + i\boldsymbol{\Gamma}^{-1}\boldsymbol{M}_{\boldsymbol{PQ}}\right)\right|^{\frac{1}{2}}. \tag{16}$$

The prefactor requires the evaluation of the stability matrix subblocks $\boldsymbol{M}_{\boldsymbol{QQ}} = \partial\mathbf{Q}_t^{(n)}/\partial\mathbf{Q}_0^{(n)}$, $\boldsymbol{M}_{\boldsymbol{PP}} = \partial\mathbf{P}_t^{(n)}/\partial\mathbf{P}_0^{(n)}$, $\boldsymbol{M}_{\boldsymbol{QP}} = \partial\mathbf{Q}_t^{(n)}/\partial\mathbf{P}_0^{(n)}$, and $\boldsymbol{M}_{\boldsymbol{PQ}} = \partial\mathbf{P}_t^{(n)}/\partial\mathbf{Q}_0^{(n)}$, which are computed along each trajectory via numerical integration of their symplectic equations of motion.[85] For this purpose, the instantaneous Hessian matrix is needed along each classical trajectory. This is the most computationally expensive part of these calculations. Specific algorithms have been developed to reduce the computational cost in high-dimensional applications.[86–88]

III. RESULTS AND DISCUSSION

A. H_2O molecule

1. Computational details

Some of us[39] recently obtained the first five vibrational eigenstates of the non-rotating water molecule using the analytical PES by Dressler and Thiel[89] with the MC SCIVR method. The eigenstates were reproduced by running five classical trajectories with initial conditions chosen according to Eq. (12) and $\delta_\alpha = 0$, i.e., with initial momenta such that the kinetic energy is equal to the harmonic vibrational energy of the corresponding harmonic states (0,0,0), (0,1,0), (0,2,0), (1,0,0), and (0,0,1). Here, the spectroscopic notation reports the symmetric, bending, and asymmetric normal mode quantum numbers, respectively. The basis set was composed of the first 11 harmonic states for each degree of freedom, implying a total of 1331 coefficients. It was shown that a good agreement with the exact Discrete Variable Representation (DVR) calculations can be achieved by dropping all the coefficients smaller than 0.01 and enforcing orthonormalization by applying the Gram–Schmidt algorithm.[39] In the present work, we compute the nuclear densities from the eigenfunctions generated with the same setup, but with a

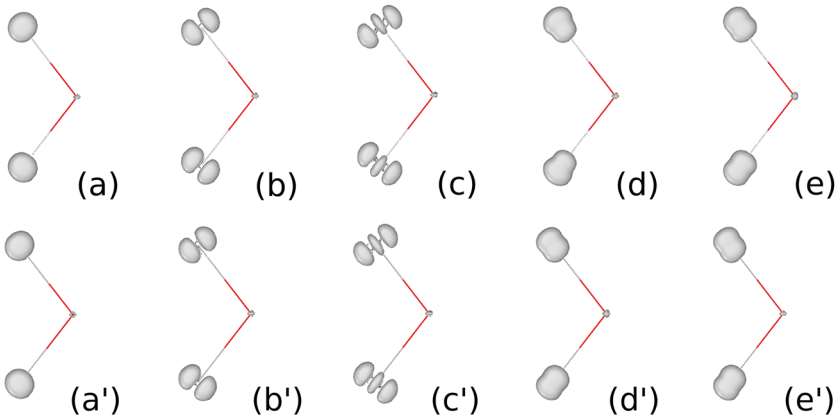

FIG. 1. Water molecule one-nucleus densities. Anharmonic vibrational state eigenfunction (000) in panel (a), (010) in panel (b), (020) in panel (c), (100) in panel (d), and (001) in panel (e). Harmonic vibrational eigenfunction (000) in panel (a′), (010) in panel (b′), (020) in panel (c′), (100) in panel (d′), and (001) in panel (e′). All isodensity surfaces are set to 10 a.u.

smaller threshold (equal to 10^{-3}) and keeping more coefficients in the harmonic base expansion. In addition, we have pruned the basis set by keeping only those basis functions, which have the same symmetry as the target eigenfunction. The coefficients are reported in the supplementary material. For the one-nucleus densities, we used bins of edge 0.0229 Å, while for the bond-length distributions, we used a bin size of 0.0077 Å, and for the angular distributions, we use a bin size of 0.45°. The Monte Carlo integration has been carried out with $L = 10^8$ steps.

2. Anharmonicity effect on nuclear densities

In Fig. 1, the one-nucleus densities of Eq. (7) for the lowest five vibrational energy eigenstates are reported. For comparison, we compute also the harmonic one-nucleus densities. The plots are shown in the water molecular plane because we do not account for rotation. First, we observe that the envelopes of the hydrogen densities are wider than the ones of the oxygen. This immediately spots the quantum nature of nuclei in molecules, whose wavefunctions are more and more delocalized as the particle mass decreases. Then, we observe the appearance of nodes as the quantum number increases; however, this is not guaranteed in the one-nucleus density representation. As already observed in the literature,[36] for the harmonic case (lower panel in Fig. 1), it is likely that the nodal structure of the wavefunction is reflected in the one-nucleus densities when normal mode atomic displacements are along a certain direction. In the water molecule case, the ground-state density correctly does not show any node. The first and second excitations of the bending mode [panels (b), (b′), (c), and (c′) in Fig. 1] have one and two nodal planes, respectively, perpendicular to the bending motion direction of the hydrogens because the bending motion is only represented by the H–O–H angle distortion. Otherwise, the first excitations of both symmetric and asymmetric stretching equally imply a motion along the two O–H bond distance directions. In this case, the nodes are not present, but just a depletion of one-nucleus density is observed where one would expect the appearance of the node.

We found a similar shape of the one-nucleus anharmonic densities (upper panels in Fig. 1). In these cases, a deformation of the lobes appears and minor differences are visible by direct comparison with the harmonic results. In particular, a slight tilting of the nodal planes of the bending modes is observed.

The difference between anharmonic and harmonic densities better clarifies the effect of the anharmonicity, as reported in Fig. 2. For the ground state density difference [panel (a) in Fig. 2], the one-nucleus density is anharmonically driven toward longer O–H bond distances, as shown by the density accumulation (red isosurface) and its corresponding density depletion (blue isosurface). Similar effects are observed for all the investigated excited states. This shows that in the anharmonic case, the equilibrium distances should be bigger than the harmonic one. In addition, for the two bending modes [panels (b) and (c)], a smaller bond angle is expected, since the bigger red lobes are localized in the inner part of the H–O–H angle. Regarding the symmetric and asymmetric stretches [panels (d) and (e)], the density differences hint at a slighter deformation toward larger H–O–H angles for the asymmetric stretch only.

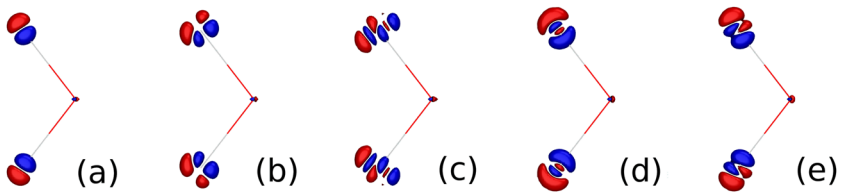

FIG. 2. Differences of the anharmonic one-nucleus density with the corresponding harmonic one. State (000) in panel (a), (010) in (b), (020) in (c), (100) in (d), and (001) in (e). Red indicates positive contributions, where the molecular density concentrates due to anharmonicity, while blue stands for the negative contributions, where the density is depleted due to anharmonicity. The isodensity surfaces are set to +5 and −5 a.u.

These qualitative observations, driven by visual inspection of density differences, are confirmed by a quantitative analysis of probability distributions of bond distances and angle amplitudes derived from the quantum harmonic, the semiclassical, and the exact quantum eigenfunctions, the latter obtained by normal-mode DVR simulations.[39] These calculations are reported in Fig. 3, where just one of the two bonding distances is plotted in the left column because of symmetry. The statistical error bars for the distributions in Fig. 3 are smaller than the linewidth. In Fig. 3, the semiclassical (red line) distributions are in good agreement with the DVR ones (blue lines). For the ground state, it is found that the average bond lengths are slightly increased for the anharmonic wavefunctions [panel (a)], while the bond angle is practically unaltered [panel (a′)]. Moreover, for all the excited states, all bond lengths are longer in the anharmonic picture with respect to the harmonic one [panels (b)–(e)]. In particular, the increase in the bond length is more significant for the two stretching modes [panels (d) and (e)]. The anharmonicity effect of O–H bonds elongation is consistent with the Morse-like shape of

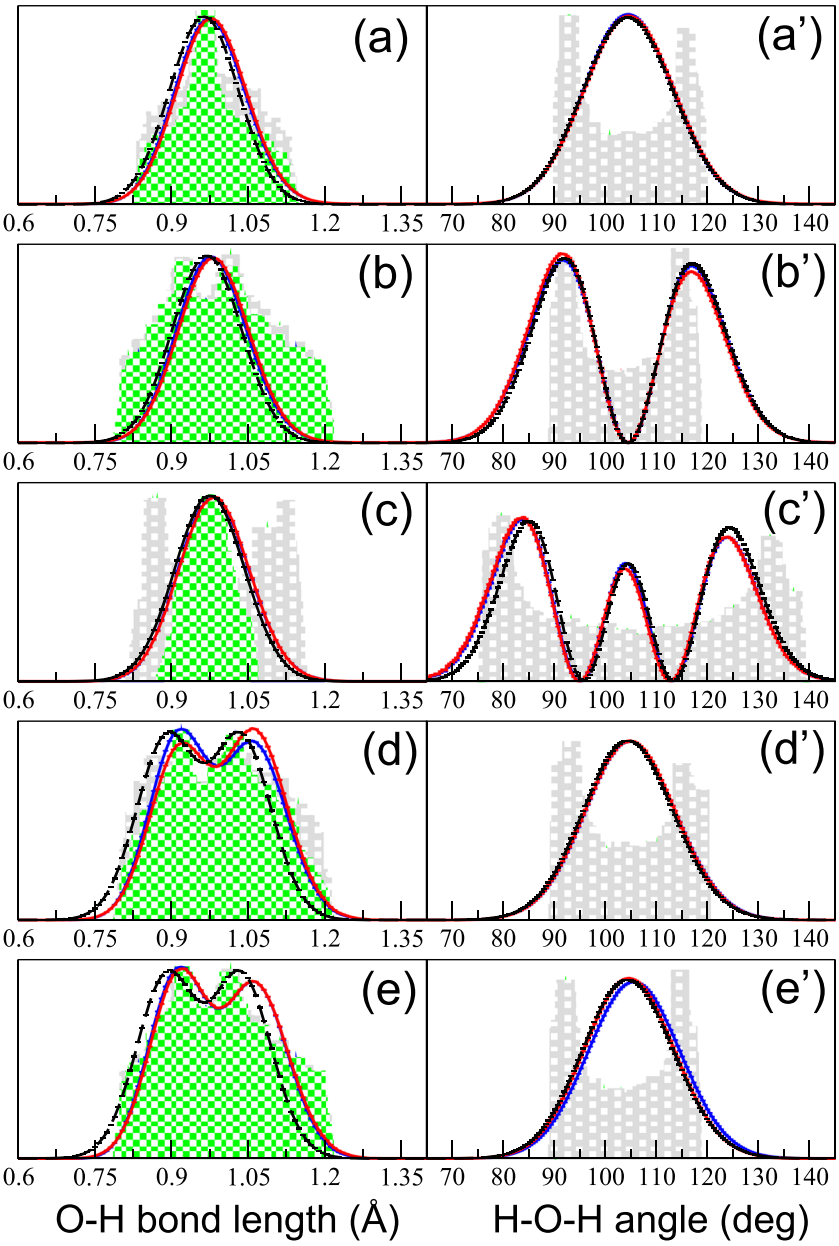

FIG. 3. Water bonds and H–O–H angle probability density distributions obtained from quantum harmonic (black dashed line), DVR[39] (blue line), and semiclassical (red line) wavefunctions. Left-hand side panels (a)–(e) are for the radial O–H distribution of the ground (000), (010), (020), (100), and (001) vibrational eigenfunctions, respectively. Right-hand side panels (a′)–(e′) are for the angular H–O–H distributions of the same ordered vibrational states. The filled-area plots on the background represent the classical distributions obtained from the classical trajectory used to generate each wavefunction with our semiclassical approach. In the left-hand side panels, gray and green histograms stand for the two bond-length distributions along each water O–H bond, and in the right panels, gray histograms are for the H–O–H angle.

the potential along the direction of the bonds. Conversely, the angle manifests a contraction only for the excited bending modes [panels (b′) and (c′)].

In the same figure, the bond length and angle distributions derived from the classical trajectories employed for the semiclassical simulation are reported as either gray or green histograms. One would expect the corresponding distribution maximum at the classical turning points if the motion along the angle or a bond corresponds exactly to the displacement of a single normal mode. This is clearly seen for all the classical H–O–H angle distributions (right-hand side panels in Fig. 3) because the angle deformation can be described by the bending mode variation only. Notice that, for all the employed EBK trajectories, we assign to the bending mode a kinetic energy corresponding at least to the harmonic zero-point energy (ZPE). In contrast, the quantum ground state and stretching excited state angle distributions are peaked around their equilibrium positions [see panels (a′), (d′), and (e′)]. Instead, for the excited bending states [panels (b′) and (c′)], the quantum mechanical distribution becomes more similar to the classical one, as the quantum number is increased. A more complicated picture arises in the bond-length distribution case (left-hand side panels of Fig. 3). The probability distributions are equal for both O–H bonds due to the symmetry of the wavefunction. However, this is not always the case for the classical distributions [green and gray histograms, see panel (c)]. This happens because our classical trajectories are short-time trajectories, as requested from the semiclassical approach, and they are too short to guarantee equilibration of the energy between the degrees of freedom of the molecule. Nevertheless, the comparison of classical distributions derived from these short trajectories is still useful to make it evident that we are able to reproduce correct quantum mechanical results starting from classical information. Indeed, the quantum distributions are always wider than the classical ones for all the considered quantities. This reveals that we are actually reproducing quantum effects because semiclassical distribution probabilities are non-zero in classical forbidden regions of the motion.

3. Anharmonicity effects on vibrational excitations

To gain deeper quantum insight into the vibrational excitations, we propose in Fig. 4 the differences between the excited state vibrational one-nucleus densities and the ground-state ones. In the upper panel, we report the differences in harmonic approximation, while in the lower panel, we report those in the anharmonic ones. Red lobes indicate density concentration, while blue lobes indicate density depletion as a consequence of the vibrational transition from the ground to the excited state. In Fig. 4, the harmonic bending excitations cause a deformation of the angle [panels (a) and (b)], while the stretching excitations deform the density along the two O–H bond directions [see panels (c) and (d)]. Here, one can see how the nuclear delocalization is wider in the overtone bending excitation [panel (b)] than in the fundamental one [panel (a)], as expected by comparison with a simple one-dimensional harmonic oscillator. This is true because the mode variation is given by a single angular variation. When the normal mode involves several geometric parameters, the nuclear density variation is not necessarily so intuitive. Asymmetric and symmetric stretching density variations look very similar because the correlations between nuclear motions

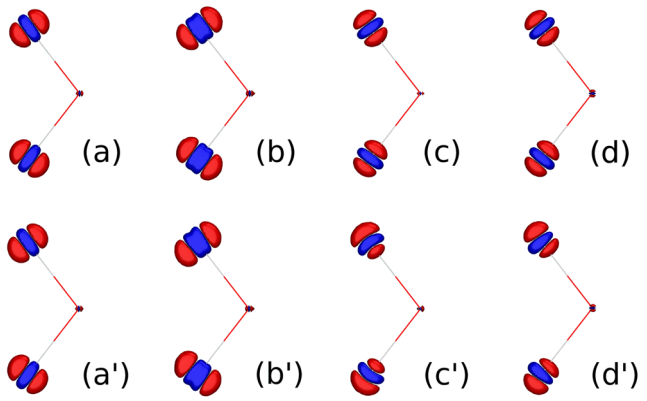

FIG. 4. Harmonic [top panels (a)–(d)] and semiclassical anharmonic [bottom panels (a′)–(d′)] nuclear density differences obtained by subtracting the zero point energy (000) state one-nucleus density to the (010), (020), (100) and (001) excited state densities, respectively. Red indicates positive contributions, where the density concentrates due to the excitation, while blue stands for the negative contributions, where the density is depleted due to the excitation. The isodensity surfaces are set to +5 and −5 a.u.

are lost in this one-nucleus density picture. However, the small deformation on the oxygen density with vertical nodal planes, which appears in panel (c), is consistent with the symmetric stretching motion, where the oxygen motion keeps the molecular center of mass fixed. In turn, for the asymmetric stretch in panel (d), the lobes on the oxygen have the nodal planes set horizontally.

The bottom panels of Fig. 4 show the anharmonic density variation after excitations. Also in this case, the shape of the lobes is influenced by the motion of the corresponding normal mode that brings the biggest contribution in the harmonic expansion of the wavefunction. Interestingly, many features show a certain amount of anharmonicity. For example, the symmetric stretch state density difference [panel (c′)] is accumulated more toward the tip of the two O–H bonds due to significant anharmonicity. In the same fashion, for the asymmetric stretch state density difference [panel (d′)], the lobes are distributed along a curved line. Finally, the fundamental and overtone bending excitation cases [panels (a′) and (b′)] are more similar to the harmonic densities, given the slightly wider lobes, with respect to the anharmonic case.

B. Protonated glycine

1. Computational details

In this section, we consider the 11-atom protonated glycine ($GlyH^+$) molecule. We are able to tackle such a system because the MC-SCIVR technique can be applied on-the-fly when fitted PESs are not available. As in our previous work,[38] we perform the quantum chemistry calculations at the DFT-B3LYP level of theory using the aug-cc-pVDZ basis set with the NWChem package.[90] The gas phase global minimum has the protonated amino group, which establishes an ionic hydrogen bond with the carbonyl oxygen.[91] The optimized structure in Fig. 5 displays C_s symmetry (see file "reference_geometry_Glyp.xyz" included in the Fortran software

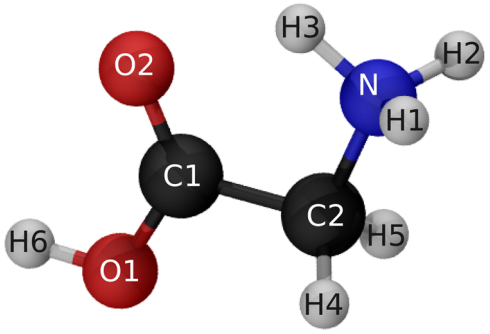

FIG. 5. Protonated glycine ($GlyH^+$) lowest energy conformer at the DFT-B3LYP/aug-cc-pVDZ level of theory.

package[92] for Cartesian coordinates), whose relevant normal-mode frequencies and symmetry characters are reported in Table I.

We focus on the 2600 cm^{-1}–3800 cm^{-1} region of the vibrational spectrum, which has been investigated experimentally to get structural information of solvated $GlyH^+$ clusters by comparison with IR spectra of the isolated-molecule.[12] Specifically, we focus on modes 23, 25, and 26, which are the IR active ones in this region, as confirmed by the Double Harmonic Approximation (DHA) in Table I. The OH stretch mode 27 is also active and we have already discussed it in our previous work.[38] We then run four on-the-fly trajectories, each one with initial conditions corresponding to the harmonic EBK prescription of the ZPE and the three fundamentals, as described in Eq. (12). Given the freedom in choosing the angle δ_α in Eq. (12), we set it equal to $\pi/2$ for normal modes 24 and 26, which correspond to the N–H1/2 and C2–H4/5 asymmetric stretches. The standard choice of $\delta_\alpha = 0$, i.e., the one for the equilibrium position, would have required a longer simulation time for observing the stretching of both bonds. Instead, with this choice, we can better explore the stretching motions during the short-time semiclassical dynamics and obtain the power spectrum displayed in Fig. 6. In the same figure, apart from the fundamentals, we can observe side peaks, which we attribute to the combination of each fundamental with the low frequency modes. However, in this work, our analysis is focused on the fundamental signals.

We write the eigenfunctions as a combination of 12 799 coefficients, after restricting the harmonic basis to the simultaneous excitation of two modes at most, with, at most, the harmonic quantum number equal to 6. The shape of the density is always determined by the largest coefficients in the harmonic expansion. By gradually dropping the smaller coefficients, we found that just those greater than 10^{-3} are significant. As in the case of water, we enforce C_s symmetry to the harmonic-basis wavefunctions. We also apply Gram–Schmidt orthonormalization between eigenfunctions starting from the ground state one. We report the largest coefficients of the states analyzed in this work and the ground state one in the supplementary material. As already discussed in our previous work,[38] the largest expansion coefficient in the ground-state function is the one of the harmonic ground state (see Table S2 of the supplementary material). Similarly, for the wavefunctions computed in this work, we find that the largest coefficients are those of the harmonic state with one quantum of energy intake for modes 23 and 26, respectively (see Table S3 of the supplementary material). As for the $\nu_{25} = 1$ anharmonic eigenfunction, there are three leading terms in the expansion whose coefficients are comparable (see Table S4 of the supplementary material). However, the harmonic state with one quantum of energy on mode 25 is the only fundamental excitation among these three harmonic states, thus determining the overall character of the wavefunction. The other two largest coefficients are combination of low frequency mode harmonic eigenfunctions.

Eventually, we represent the one-nucleus density with a histogram of 3D cubes with the edge equal to 0.049 Å. The Monte Carlo integration has been carried out with $L = 10^8$ steps. We also obtained all the bond-length, angle, and dihedral densities with both harmonic and anharmonic wavefunctions for all the considered states, with typical resolutions of 0.008 Å, 0.45°, and 0.45°, respectively.

2. Anharmonicity effect on nuclear densities

In this paragraph, we analyze, with the aid of the calculated one-nucleus densities, the bond, angle, and dihedral distributions and the effect of the inclusion of anharmonicity in the excited vibrational states of $GlyH^+$. For the sake of brevity, we only show some selected bond-length distributions in the main text. Additional distributions are reported in the supplementary material, when useful to support the discussion.

We start from the excited vibrational state $\nu_{23} = 1$, where the inclusion of anharmonicity shows a less mobile H3. This localization is evident from the isodensity plot in panel (a) of Fig. 7, where the anharmonic accumulation of the H3 one-nucleus density toward the center of the distribution is spotted by a red lobe with two symmetric blue lobes at the side. We better render this feature by looking at the N–H3 and C2–H4/5 bond-length distributions reported in

TABLE I. The six highest fundamental frequencies (ω_α) for the protonated glycine ($GlyH^+$) at the DFT-B3LYP/aug-cc-pVDZ level of theory together with their symmetry group Irreducible Representation (Irr. Repr.) and their Double Harmonic Approximation (DHA) IR intensities.

α-th normal mode	ω_α (cm^{-1})	Description	Irr. repr.	DHA IR intensity (a.u.)
22	3105	N–H3 stretch + C2–H4/5 symmetric stretch in phase	A′	0.804
23	3117	N–H3 stretch + C2–H4/5 symmetric stretch out of phase	A′	4.580
24	3170	C2–H4/5 asymmetric stretch	A″	0.123
25	3445	N–H1/2 symmetric stretch	A′	2.882
26	3505	N–H1/2 asymmetric stretch	A″	2.718
27	3693	O1–H6 stretch	A′	4.263

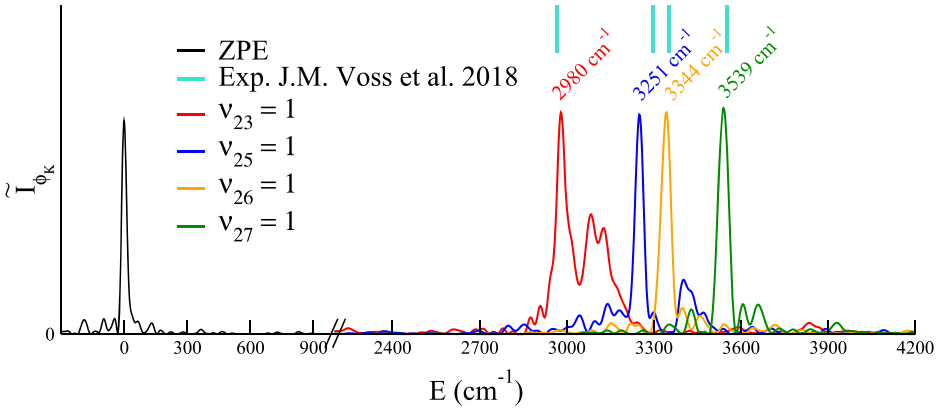

FIG. 6. GlyH$^+$ MC-SCIVR power spectrum. Each peak is obtained from a trajectory with the energy equal to the fundamental modes 23, 25, 26, and 27 using the initial conditions of Eq. (12) and the relative harmonic reference state.[46] The peak positions are shown relative to the ZPE one, and the peak heights have been arbitrarily scaled, since we are interested on peak positions only, i.e., E_n in Eq. (14). The ZPE and ν_{27} peaks are taken from our previous study.[38] Vertical lines are the peak positions from the experimental IR spectrum of Voss, Fischer, and Garand.[12]

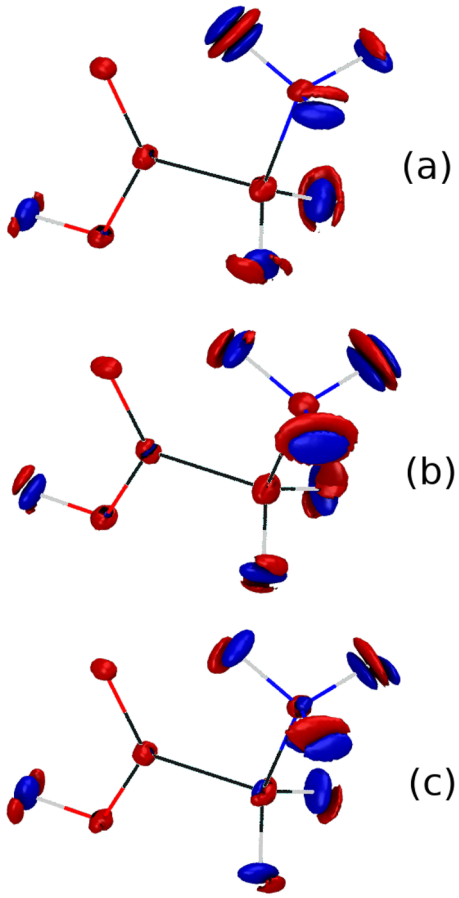

FIG. 7. One-nucleus density differences between the anharmonic and the corresponding harmonic marginal one-nucleus density for the (a) ν_{23} = 1, (b) ν_{25} = 1, and (c) ν_{26} = 1 vibrational excited states. Red indicates positive contributions, where the density concentrates due to anharmonicity, while blue stands for the negative contributions, where the density is depleted due to anharmonicity. The isodensity surfaces are set to +0.15 and −0.15 a.u., respectively

panels (a) and (a′) of Fig. 8. The C2–H4/5 bond length is increased with respect to the ground state and the harmonic case and the H4–C2–H5 angle is larger (see Fig. S1 in the supplementary material). A strong anharmonic effect is observed in panel (a) of Fig. 8 for the N–H3 bond. Here, the harmonic double peak distribution becomes a single peak upon anharmonicity inclusion. In the harmonic case, normal mode 23 has a significant displacement vector lying along the N–H3 bond direction. This movement counterbalances the symmetric C2–H4/5 stretch to keep the center of mass of the molecule fixed. We can model the oscillation along the N–H3 as a one-dimensional harmonic oscillator, and we observe the appearance of a node in the probability distribution by giving one quantum of excitation, consistently with the one-dimensional harmonic oscillator model. Instead, in the anharmonic picture, the oscillation along the N–H3 bond is no longer separable from other motions. Anharmonicity mixes normal mode 23 with other mode contributions, and the associated displacements of the N and H3 nuclei no longer lie along the bond direction. As a consequence, no clear nodal feature is found upon excitation.

For both the ν_{25} = 1 and ν_{26} = 1 excited states [panels (b) and (c) of Fig. 7], the most evident anharmonic effect is the localization of the one-nucleus density on the H1/2 nuclei. This apparently contradictory feature is explained by the appearance of a single peak distribution for the N–H1/2 bond lengths in the anharmonic picture, as shown in panels (b) and (c) of Fig. 8. The N–H1/2 symmetric and asymmetric stretches can be compared to the water symmetric and asymmetric stretches described above. From the normal-mode point of view, they behave similarly because normal modes 25 and 26 involve exclusively two H atoms distance variations without any angle changes. However, the inclusion of anharmonicity acts differently for the amino group. For water, we observe that the harmonic and anharmonic bond-length distributions have the same double peak shape [panels (d) and (e) in Fig. 3], while for GlyH$^+$, the distributions become single-peaked in the anharmonic case [panels (a)–(c) in Fig. 8], showing once again that both ν_{25} = 1 and ν_{26} = 1 excitation dynamics involve several atoms and not only the N–H1/2 and N–H3 distances. Therefore, the inclusion of anharmonicity in the eigenfunction highlights the couplings between these N–H stretches and other modes. In particular, we find for both modes a significant coupling to the breathing of the O2–C1–C2–N–H3 ring of atoms. Concerning mode 25, there is a general broadening of bond length

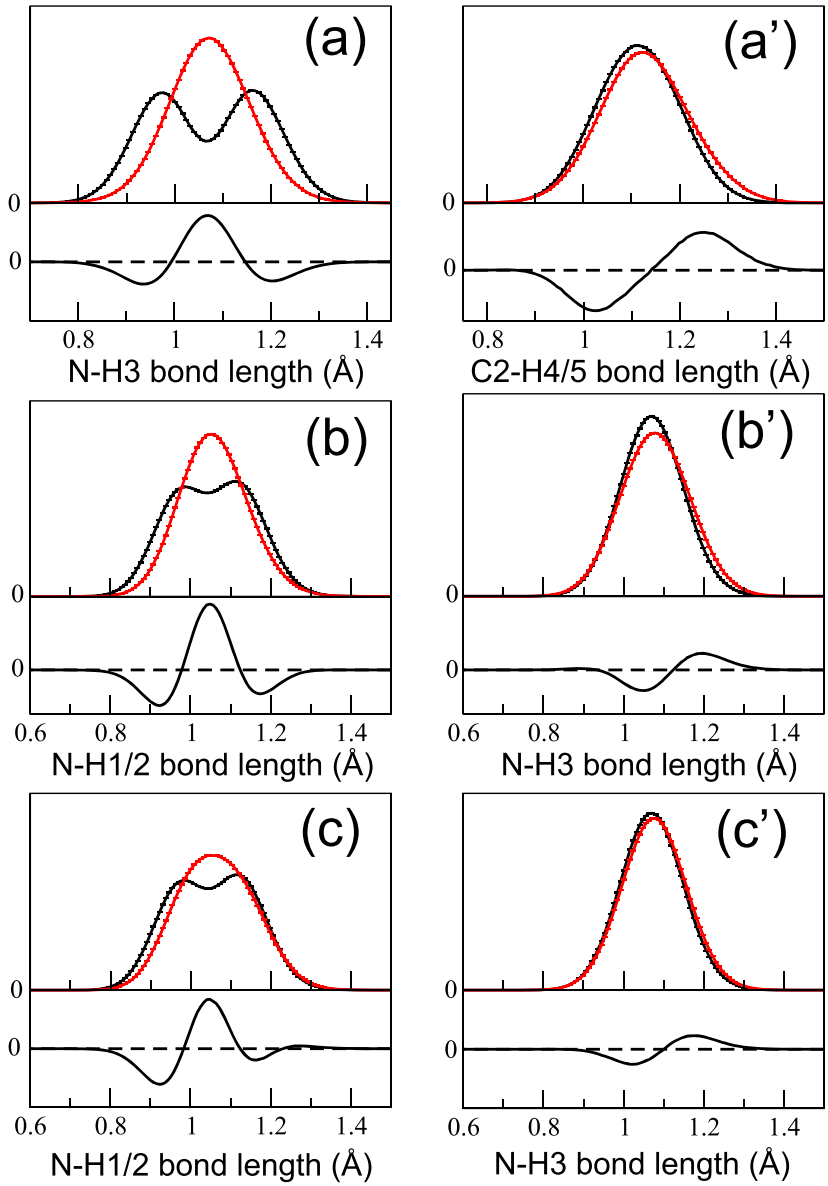

FIG. 8. Bond-length distributions comparison between harmonic (black lines) and anharmonic (red lines) states for excitation ν_{23} = 1 along the N–H3 and C2–H4/5 stretching [panels (a) and (a′)], ν_{25} = 1 along N–H1/2 and N–H3 ones [panels (b) and (b′)], and ν_{26} = 1 along N–H1/2 and N–H3 directions [panels (c) and (c′)]. The lower part of each plot shows the difference of the two curves reported in the upper part by subtracting the harmonic distribution from the anharmonic one.

and angles distributions for the ring structure. At the same time, a clear reduction of the O2–C1–C2 and C1–C2–N angles is observed, while the N–H3 bond becomes longer [Fig. 8, panel (b′)]. However, asymmetric stretch state 26 predicts a deformation of the ring structure by shortening the O2–H3 distance and elongating the C1–C2 backbone bond. At the same time, we observe that the C2–N bond becomes shorter and the N–H3 longer [Fig. 8, panel (c′)]. All these considerations suggest that the introduction of anharmonicity for both states leads to a picture where the H3 is increasingly shared with the O2 atom of the carbonyl group. Finally, we note that the broadening of the dihedral angles distributions are complementary in the two states. More specifically, in the ν_{25} = 1 eigenstate, the dihedrals distributions for the "carboxylic end" of the molecule are equal to the harmonic ones, while the dihedral distributions for the "aminic end" result slightly broadened. Instead, for the ν_{26} = 1 eigenstate, the effect is the opposite, since anharmonicity introduces a significant broadening of the distributions for the carboxyl part of $GlyH^+$. All these information is well summarized by the isodensity plots in Fig. 7.

3. Anharmonicity effect on vibrational excitations

We now look at the one-nucleus density differences between excited vibrational states and the ground one, both using the harmonic and anharmonic eigenfunctions. We will show that a

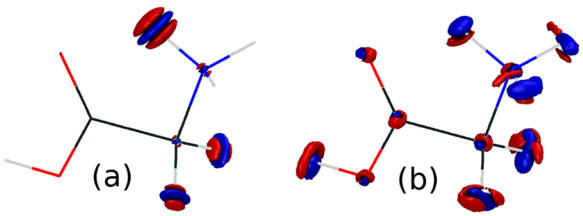

FIG. 9. $GlyH^+$ one-nucleus density difference plots for the ν_{23} = 1 vibrational eigenstate. Panel (a) depicts the difference between excited and ground harmonic densities, while panel (b) shows the anharmonic case. Red indicates positive contributions, while blue stands for the negative contributions. All isodensities are set to +0.1 and −0.1 a.u.

significant wavefunction spreading under excitations over the molecular structure occurs for all the considered anharmonic eigenstates, at variance with the harmonic ones.

Panel (a) of Fig. 9 and panels (a) and (a′) of Fig. 10 show the one-nucleus density differences in harmonic approximation for the case ν_{23} = 1. The harmonic isodensity difference plot shows lobes on the H3 nucleus, meaning that this vibrational mode has its major contribution on the N–H3 stretching and a minor one on the two C1–H4/5 stretches, as shown in panel (a) of Fig. 9. In Fig. 10, in the harmonic case (left panels), the N–H3 bond-length distribution is a single peak around equilibrium, while it becomes a double peak in the excited state ν_{23} = 1 [panel (a)]. On the contrary, the C2–H4/5 bond-length distribution is single-peaked both in the ground and in the excited state [panel (a′)]. This agrees with the harmonic normal-mode picture, where the bigger displacements in Cartesian coordinates are found along the N–H3 bond direction.

The semiclassical anharmonic eigenfunctions show instead quite a different pattern, and the harmonic node is not present in the anharmonic excitation. As before, this is because the excitation involves several modes and the reasoning based on the harmonic mode excitation is not meaningful anymore. This is really apparent by inspection of Fig. 9. In the harmonic case, the density deformation is confined to the displacements related to normal mode 23, while in the semiclassical anharmonic picture, the one-nucleus

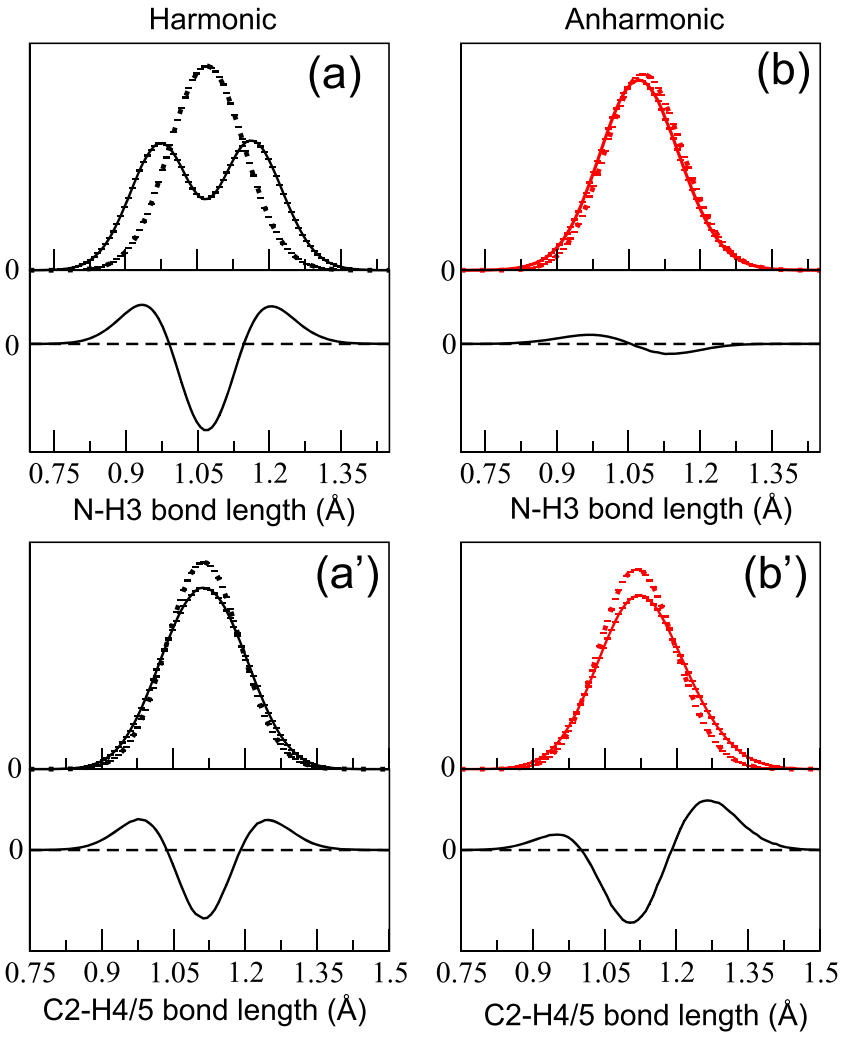

FIG. 10. The ν_{23} = 1 excited state (continuous lines) and the ground state (dotted lines) bond-length distributions. Panels (a) and (a′) in harmonic approximation along the N–H3 and C2–H4/5 stretch directions, respectively. Panels (b) and (b′) show the anharmonic case. The ground state densities are presented in our previous work.[38] The lower parts of the plots show the difference of the curves reported in the upper parts.

density change is distributed all over the molecular structure. One can appreciate this by looking at the red lobes along the backbone structure in the anharmonic excitation in Fig. 9. In the semiclassical anharmonic picture, the $\nu_{23} = 1$ excitation includes a density change for the far-away O1–H6 stretch displacement as well. The two-lobe shape on H3 in this picture can be better understood by looking at bond-length distributions in Fig. 10. Panel (b) reports a single-peak distribution for the N–H3 bond length also for the excited state, differently from the harmonic double peak one. The three-lobe shape on H4/5 is instead qualitatively equivalent to the harmonic one, as it is observed for the C2–H4/5 bond-length distributions [panel (a′) and panel (b′)]. This evidence proves a strong coupling between the oscillation along N–H3 bond and the other modes in the anharmonic picture, and a weaker coupling of the C2–H4/5 stretches with the other motions.

Moving to higher frequency modes, the density differences in harmonic approximation indicates a very neat effect on the N–H1/2 bond oscillations for the $\nu_{25} = 1$ and $\nu_{26} = 1$ states, as reported in panels (a) and (a′) of Fig. 11. This is consistent with the classical normal-mode displacements. In the same pictures, the symmetric and asymmetric N–H1/2 stretches could be distinguished only by looking at the small contributions on the N nucleus where the distortion in the N one-nucleus density in the symmetric stretch case is parallel to the main distortion found on the H1/2 nuclei [panel (a)]. The reason is that, as already pointed out in the case of the water molecule, the molecule has to keep its center of mass fixed while undergoing a symmetric stretch. A perpendicular distortion is present in the N–H1/2 asymmetric stretch [panel (a′)]. Turning our attention to the anharmonic excitations [see panel (b) and panel (b′) of Fig. 11], the spreading of the excitations over the whole structure is once again the main feature. The excitation of the eigenstate $\nu_{25} = 1$ has a less evident stretching character than the $\nu_{26} = 1$. In other words, the anharmonic lobe pattern of the H1 and H2 atoms of the amino group is more similar to the harmonic ones for the $\nu_{26} = 1$ eigenfunction than for the $\nu_{25} = 1$ state. Nevertheless, the two states can be distinguished using the same reasoning applied to the harmonic excitations. Specifically, the nodal planes of the two H nuclei in the amino group are set perpendicularly to the bond axes in the case of the symmetric stretch, while for the asymmetric stretch, they are set parallel. Another feature of the anharmonic excitations is the shortening of O2–H3 distances, which is more pronounced for the $\nu_{25} = 1$ eigenstate. This is indicated by the position of the two anharmonic density accumulations on the O2 and H3 nuclei, and it is also confirmed by the corresponding bond-length distribution. In the harmonic picture, the O2–H3 distance reduction is completely missed. There, the mode related to this intermolecular rearrangement is the N–H3 stretch mode 23, which instead loses this local character in the anharmonic picture, as discussed in the previous paragraph.

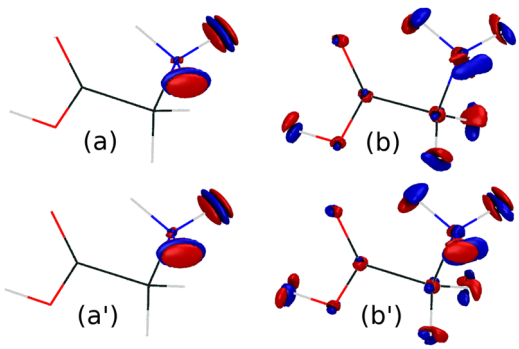

FIG. 11. One-nucleus density difference plots for the $GlyH^+$ $\nu_{25} = 1$ [panels (a) and (b)] and $\nu_{26} = 1$ [panels (a′) and (b′)] vibrational eigenstates. Panels (a) and (a′) depict the difference of the harmonic excited state and ground state densities, while panels (b) and (b′) refer to the anharmonic case. Red indicates positive contributions, while blue stands for the negative contributions. All isodensities are set to 0.1 a.u. and −0.1 a.u.

IV. SUMMARY AND CONCLUSIONS

In this paper, we have detailed how semiclassical eigenfunctions,[39,53] which are written as combinations of products of one-dimensional harmonic vibrational eigenfunctions, can be profitably employed for nuclear density calculations. Specifically, we calculate the marginal one-nucleus density, also the bond-length, angle and dihedral distributions using a Monte Carlo integration over the remaining nuclei positions. Given the state of the art where one-nucleus densities are given in harmonic approximation,[36] our semiclassical approach calculates the nuclear densities, including anharmonic and quantum mechanical effects. The method is based on classical trajectories and it is implemented either on a pre-computed PES or on-the-fly, i.e., using an *ab initio* molecular dynamics approach.[93]

We take the water molecule as a benchmark for checking the accuracy of our nuclear densities and get familiar with this quantum mechanical nuclear representation. We observe the quantum harmonic description to be quite accurate in this case and similar to the semiclassical and exact anharmonic ones by reproducing all main quantum features.

We then calculate protonated glycine molecule nuclear densities, complementing our previous work.[38] In this case, no PES is available, and our semiclassical calculations are performed by running classical trajectories on-the-fly using the NWChem suite of codes. We find, in this case, the coupling to be strong and the picture provided by the harmonic approximation of the normal modes to be oversimplified, since excitations are typically spread all over the molecular structure. For example, vibrational excitations $\nu_{25} = 1$ and $\nu_{26} = 1$ in a normal-mode picture are described only by vibrational excitations of the amino group, i.e., N–H1/2 stretching displacements. Instead, in the quantum mechanical picture provided by our semiclassical nuclear densities, all atoms are significantly affected and we find even a strong involvement of the O1–H6 stretch, which is located at the other end of the molecule.

In the case of water molecule, we also point out that a classical density distribution obtained using the same trajectories employed for the semiclassical simulations is inadequate for the low quantum number vibrational state density description and it becomes more suitable as the number of quanta of excitation are increased.

Finally, we find that, when considering significantly anharmonic states, the three-dimensional (3D) one-nucleus densities are usefully complemented by the distributions of internal coordinates, such as bond lengths, angles, and dihedrals, because they focus more

on local distortions. We expect that the methodology presented here will provide insightful information also for more flexible molecules, especially when considering the densities pertaining to rigid modes, provided a judicious sampling of the floppy modes will be enacted.[65]

In summary, the quantum mechanical tool presented in this paper allows us to show and quantify for both ground and vibrational excited states how much nuclear densities and nuclear motion, in general, deviate from a harmonic description.

SUPPLEMENTARY MATERIAL

See the supplementary material for the list of coefficients of the water and protonated glycine vibrational wavefunctions and plots of additional distributions of the protonated glycine molecule useful to support the discussion. We also provide a Fortran software package[92] with instructions for the reproduction of the results for both water and $GlyH^+$.

ACKNOWLEDGMENTS

The authors thank Dr. F. Gabas for contribution in the early stages of this work. The authors acknowledge financial support from the European Research Council (ERC) under the European Union's Horizon 2020 research and innovation programme (Grant Agreement No. 647107—SEMICOMPLEX—ERC-2014-CoG) and the Italian Ministry of Education, University, and Research (MIUR; FARE Programme No. R16KN7XBRB-project QURE). Part of the needed CPU time was provided by CINECA (Italian Supercomputing Center) under ISCRAB project "QUASP" and ISCRAC project "MCSCMD."

DATA AVAILABILITY

The data that support the findings of this study are openly available in Zenodo at http://doi.org/10.5281/zenodo.4046872.[92]

REFERENCES

[1] R. Fausto, G. O. Ildiz, E. M. Bras, and B. A. Nogueira, *Molecular Spectroscopy-Experiment and Theory* (Springer, 2019), pp. 199–222.
[2] D. Gerlich, J. Chin. Chem. Soc. **65**, 637 (2018).
[3] J. Roithová, A. Gray, E. Andris, J. Jašík, and D. Gerlich, Acc. Chem. Res. **49**, 223 (2016).
[4] A. P. Cismesia, L. F. Tesler, M. R. Bell, L. S. Bailey, and N. C. Polfer, J. Mass Spectrom. **52**, 720 (2017).
[5] A. B. Wolk, C. M. Leavitt, E. Garand, and M. A. Johnson, Acc. Chem. Res. **47**, 202 (2013).
[6] K. R. Asmis, A. Fielicke, G. von Helden, and G. Meijer, Chem. Phys. Solids Their Surf. **12**, 327 (2007).
[7] M. Quack, Annu. Rev. Phys. Chem. **41**, 839 (1990).
[8] T. R. Rizzo and O. V. Boyarkin, *Gas-Phase IR Spectroscopy and Structure of Biological Molecules* (Springer, 2014), pp. 43–97.
[9] H. Schwarz and K. R. Asmis, Chem. - Eur. J. **25**, 2112 (2019).
[10] E. Garand, J. Phys. Chem. A **122**, 6479 (2018).
[11] M. A. Czarnecki, Y. Morisawa, Y. Futami, and Y. Ozaki, Chem. Rev. **115**, 9707 (2015).
[12] J. M. Voss, K. C. Fischer, and E. Garand, J. Phys. Chem. Lett. **9**, 2246 (2018).
[13] K. R. Asmis and D. M. Neumark, Acc. Chem. Res. **45**, 43 (2011).
[14] M. F. Bush, R. J. Saykally, and E. R. Williams, J. Am. Chem. Soc. **129**, 2220 (2007).
[15] M. Y. Choi and R. E. Miller, J. Am. Chem. Soc. **128**, 7320 (2006).
[16] F. Gabas, G. Di Liberto, R. Conte, and M. Ceotto, Chem. Sci. **9**, 7894 (2018).
[17] B. C. Stipe, M. A. Rezaei, and W. Ho, Science **280**, 1732 (1998).
[18] S. Duan, G. Tian, and Y. Luo, Angew. Chem., Int. Ed. **55**, 1041 (2016).
[19] P. Liu, D. V. Chulhai, and L. Jensen, ACS Nano **11**, 5094 (2017).
[20] J. Lee, K. T. Crampton, N. Tallarida, and V. A. Apkarian, Nature **568**, 78 (2019).
[21] A. M. Carrascosa, T. Northey, and A. Kirrander, Phys. Chem. Chem. Phys. **19**, 7853 (2017).
[22] F. Teixeira and M. N. D. S. Cordeiro, J. Chem. Theory Comput. **15**, 456 (2018).
[23] J. M. Bowman, Acc. Chem. Res. **19**, 202 (1986).
[24] R. Gerber and M. A. Ratner, Adv. Chem. Phys. **70**, 97 (1988).
[25] I. Kosztin, B. Faber, and K. Schulten, Am. J. Phys. **64**, 633 (1996).
[26] O. Christiansen, Phys. Chem. Chem. Phys. **9**, 2942 (2007).
[27] O. Christiansen, Phys. Chem. Chem. Phys. **14**, 6672 (2012).
[28] J. S. Mancini and J. M. Bowman, J. Phys. Chem. Lett. **5**, 2247 (2014).
[29] A. B. McCoy, Int. Rev. Phys. Chem. **25**, 77 (2006).
[30] J. M. Bowman, T. Carrington, and H.-D. Meyer, Mol. Phys. **106**, 2145 (2008).
[31] E. Mátyus, J. Šimunek, and A. G. Császár, J. Chem. Phys. **131**, 074106 (2009).
[32] K. Ruud, P.-O. Åstrand, and P. R. Taylor, J. Chem. Phys. **112**, 2668 (2000).
[33] P.-O. Åstrand, K. Ruud, and P. R. Taylor, J. Chem. Phys. **112**, 2655 (2000).
[34] O. Vendrell, F. Gatti, and H.-D. Meyer, J. Chem. Phys. **127**, 184303 (2007).
[35] M. Ceotto, S. Valleau, G. F. Tantardini, and A. Aspuru-Guzik, J. Chem. Phys. **134**, 234103 (2011).
[36] A. Schild, Front. Chem. **7**, 424 (2019).
[37] T. Culpitt, Y. Yang, F. Pavošević, Z. Tao, and S. Hammes-Schiffer, J. Chem. Phys. **150**, 201101 (2019).
[38] C. Aieta, M. Micciarelli, G. Bertaina, and M. Ceotto, Nat. Commun. **11**, 4348 (2020).
[39] M. Micciarelli, R. Conte, J. Suarez, and M. Ceotto, J. Chem. Phys. **149**, 064115 (2018).
[40] W. Humphrey, A. Dalke, and K. Schulten, J. Mol. Graphics **14**, 33 (1996).
[41] A. L. Kaledin and W. H. Miller, J. Chem. Phys. **118**, 7174 (2003).
[42] A. L. Kaledin and W. H. Miller, J. Chem. Phys. **119**, 3078 (2003).
[43] M. Ceotto, S. Atahan, G. F. Tantardini, and A. Aspuru-Guzik, J. Chem. Phys. **130**, 234113 (2009).
[44] M. Ceotto, S. Atahan, S. Shim, G. F. Tantardini, and A. Aspuru-Guzik, Phys. Chem. Chem. Phys. **11**, 3861 (2009).
[45] M. Ceotto, D. Dell'Angelo, and G. F. Tantardini, J. Chem. Phys. **133**, 054701 (2010).
[46] M. Ceotto, G. F. Tantardini, and A. Aspuru-Guzik, J. Chem. Phys. **135**, 214108 (2011).
[47] R. Conte, A. Aspuru-Guzik, and M. Ceotto, J. Phys. Chem. Lett. **4**, 3407 (2013).
[48] D. Tamascelli, F. S. Dambrosio, R. Conte, and M. Ceotto, J. Chem. Phys. **140**, 174109 (2014).
[49] R. P. Feynman and A. R. Hibbs, *Quantum Mechanics and Path Integrals* (McGraw-Hill, 1965).
[50] J. Liu, W. H. Miller, G. S. Fanourgakis, S. S. Xantheas, S. Imoto, and S. Saito, J. Chem. Phys. **135**, 244503 (2011).
[51] X. Liu and J. Liu, Mol. Phys. **116**, 755 (2018).
[52] N. V. Golubev, T. Begusic, and J. Vanicek, Phys. Rev. Lett. **125**, 083001 (2020).
[53] M. Micciarelli, F. Gabas, R. Conte, and M. Ceotto, J. Chem. Phys. **150**, 184113 (2019).
[54] T. Begusic and J. Vanicek, J. Chem. Phys. **153**, 024105 (2020).
[55] M. Ceotto, G. Di Liberto, and R. Conte, Phys. Rev. Lett. **119**, 010401 (2017).
[56] F. Gabas, R. Conte, and M. Ceotto, J. Chem. Theory Comput. **13**, 2378 (2017).
[57] G. Di Liberto, R. Conte, and M. Ceotto, J. Chem. Phys. **148**, 014307 (2018).
[58] G. Di Liberto, R. Conte, and M. Ceotto, J. Chem. Phys. **148**, 104302 (2018).
[59] X. Ma, G. Di Liberto, R. Conte, W. L. Hase, and M. Ceotto, J. Chem. Phys. **149**, 164113 (2018).
[60] M. Buchholz, F. Grossmann, and M. Ceotto, J. Chem. Phys. **148**, 114107 (2018).

[61] M. Buchholz, F. Grossmann, and M. Ceotto, J. Chem. Phys. **147**, 164110 (2017).
[62] M. Buchholz, F. Grossmann, and M. Ceotto, J. Chem. Phys. **144**, 094102 (2016).
[63] F. Gabas, G. Di Liberto, and M. Ceotto, J. Chem. Phys. **150**, 224107 (2019).
[64] F. Gabas, R. Conte, and M. Ceotto, J. Chem. Theory Comput. **16**, 3476 (2020).
[65] G. Bertaina, G. Di Liberto, and M. Ceotto, J. Chem. Phys. **151**, 114307 (2019).
[66] M. Cazzaniga, M. Micciarelli, F. Moriggi, A. Mahmoud, F. Gabas, and M. Ceotto, J. Chem. Phys. **152**, 104104 (2020).
[67] R. Pérez de Tudela and D. Marx, J. Phys. Chem. Lett. **7**, 5137 (2016).
[68] E. B. Wilson, J. C. Decius, and P. C. Cross, *Molecular Vibrations: The Theory of Infrared and Raman Vibrational Spectra* (Courier Corporation, 1980).
[69] G. E. P. Box and M. E. Muller, Ann. Math. Stat. **29**, 610 (1958).
[70] R. G. Parr and W. Yang, Annu. Rev. Phys. Chem. **46**, 701 (1995).
[71] A. Blondel and M. Karplus, J. Comput. Chem. **17**, 1132 (1996).
[72] J. B. Keller, Ann. Phys. **4**, 180 (1958).
[73] E. J. Heller, J. Chem. Phys. **75**, 2923 (1981).
[74] E. J. Heller, Acc. Chem. Res. **14**, 368 (1981).
[75] E. J. Heller, J. Chem. Phys. **94**, 2723 (1991).
[76] W. H. Miller, J. Chem. Phys. **53**, 1949 (1970).
[77] M. F. Herman and E. Kluk, Chem. Phys. **91**, 27 (1984).
[78] K. G. Kay, J. Chem. Phys. **100**, 4377 (1994).
[79] K. G. Kay, J. Chem. Phys. **101**, 2250 (1994).
[80] K. G. Kay, J. Chem. Phys. **100**, 4432 (1994).
[81] S. V. Antipov, Z. Ye, and N. Ananth, J. Chem. Phys. **142**, 184102 (2015).
[82] M. S. Church, S. V. Antipov, and N. Ananth, J. Chem. Phys. **146**, 234104 (2017).
[83] M. Wehrle, M. Šulc, and J. Vaníček, J. Chem. Phys. **140**, 244114 (2014).
[84] M. Wehrle, S. Oberli, and J. Vaníček, J. Phys. Chem. A **119**, 5685 (2015).
[85] M. L. Brewer, J. S. Hulme, and D. E. Manolopoulos, J. Chem. Phys. **106**, 4832 (1997).
[86] Y. Zhuang, M. R. Siebert, W. L. Hase, K. G. Kay, and M. Ceotto, J. Chem. Theory Comput. **9**, 54 (2013).
[87] M. Ceotto, Y. Zhuang, and W. L. Hase, J. Chem. Phys. **138**, 054116 (2013).
[88] R. Conte, F. Gabas, G. Botti, Y. Zhuang, and M. Ceotto, J. Chem. Phys. **150**, 244118 (2019).
[89] S. Dressler and W. Thiel, Chem. Phys. Lett. **273**, 71 (1997).
[90] M. Valiev, E. J. Bylaska, N. Govind, K. Kowalski, T. P. Straatsma, H. J. J. Van Dam, D. Wang, J. Nieplocha, E. Apra, T. L. Windus, and W. A. de Jong, Comput. Phys. Commun. **181**, 1477 (2010).
[91] K. Zhang and A. Chung-Phillips, J. Comput. Chem. **19**, 1862 (1998).
[92] C. Aieta, G. Bertaina, M. Micciarelli, and M. Ceotto (2020). "Semiclassical nuclear density," Zenodo. http://doi.org/10.5281/zenodo.4046872
[93] R. Conte, G. Botti, and M. Ceotto, Vib. Spectrosc. **106**, 103015 (2020).